

SPARSITY-BASED SIMPLIFICATION OF SPECTRAL-DOMAIN OPTICAL COHERENCE TOMOGRAPHY IMAGES OF CARDIAC SAMPLES

William Meinie^{1,2}, Yu Gan³, Christine P. Hendon³,
Jean-Christophe Olivo-Marin², Andrew Laine⁴, and Elsa D. Angelini^{1,4}

¹LTCI, CNRS, Telecom ParisTech, Universite Paris-Saclay, France

²Institut Pasteur, Unité d'Analyse d'Images Biologiques, France

³Department of Electrical Engineering, Columbia University, New York, NY, USA

⁴Department of Biomedical Engineering, Columbia University, New York, NY, USA

ABSTRACT

We propose a sparsity-based simplification method for Spectral Domain Optical Coherence Tomography (SD-OCT) images of cardiac samples, displaying layers of tissue. Inspired by the Compressed Sensing (CS) theory, we implement a dedicated sparse sampling of SD-OCT samples achieving image simplification suited for layers segmentation, which is the target application. We compare our simplified images to state of the art denoising approaches. We also validate a straightforward segmentation approach on the variance map of the simplified images against manual delineation on raw SD-OCT images of *in-vitro* biological samples from four human hearts. Finally, we correlate average layer thickness with histopathological measures.

Index Terms— Optical Coherence Tomography, Sparse sampling, Image simplification, Image segmentation.

1. INTRODUCTION

Optical coherence tomography (OCT) has emerged as a promising image modality to characterize biological tissues. With axial/lateral resolutions at micron-level, OCT images provide detailed morphological information and enable applications such as optical biopsy and virtual histology for clinical needs. Meanwhile, for the application of morphological segmentation, it is expected to enhance only the boundary information, rather than to enrich detailed tissue information. There is a need to simplify OCT images such that the images are smoothed while boundary contours are enhanced.

In this work we focus on *in-vitro* spectral domain optical coherence tomography (SD-OCT) images of cardiac samples and their segmentation. In the human myocardium, tissues are organized in layers (collagen, endothelium, and myocardium) and a large portion of OCT data is redundant while corrupted by speckle noise. As presented in [1], there are two types of speckle in OCT: one is signal-degrading (the noise) and the other one is signal-carrying (enhances information about structures in the tissues). A data simplification scheme, targeting data denoising during image sampling is proposed to make cardiac tissue layers extraction simpler. As a result, our scheme tends to reduce both types of speckle noise, which leads to a loss of information about the struc-

tures inside the tissues. This is not an issue, as we focus on layers extraction in this work. This constitutes a radically different approach from the trend in retinal OCT imaging to design specialized layer segmentation methods such as [2, 3, 4] which might not work on pathological images and require careful parameter tuning and sometimes learning.

Inspired by the Compressed Sensing (CS) theory [5], we propose an image simplification method that exploits the sparsity of structural details in OCT images. Sparsity of SD-OCT images was used for denoising in [6], training on high SNR images and ending up in a quite long run time. The use of CS in SD-OCT has been studied in [7], where the authors proved that it is possible to reconstruct OCT images using only a fraction of the CCD camera pixels. Their method exploited 1D-Fourier transforms of the samples, used for acquisition, but did not exploit the 2D structure of the layers. In addition, their method aimed at reconstructing the exact image, and was only tested on noise-free data.

Multiple denoising methods have been proposed for OCT images as in [8, 9]. Multiple methods also exist for image denoising in general, in particular state of the art methods tested in the Results section.

Here, our objective is to simplify SD-OCT myocardial images while preserving detailed information on layers toward tissue segmentation. The approach consists in generating a simplified estimator \hat{x} of the true image x , from a noisy observation $y = \Phi x$, by enhancing piecewise constant areas in the image. The sparsity of the estimator is enforced via minimization of the Total-Variation (TV) norm [10]: $\|x\|_{TV} = \sum_{p,q} \sqrt{\partial_h x(p,q)^2 + \partial_v x(p,q)^2}$ where $\partial_h x$ and $\partial_v x$ are the partial horizontal and vertical derivatives of the image x , and p, q are the pixels coordinates.

2. SPARSITY-BASED ADAPTIVE SIMPLIFICATION

Introduced in [11], we use a CS-based estimation of the image data exploiting the denoising capacity of the TV sparsity constraint and the redundancies of multiple reconstructions using different random sampling patterns in Fourier. Instead of targeting denoising as in [11], we target here image simplification for layers enhancement via specific tuning of the Fourier sampling patterns and the parameters of the method.

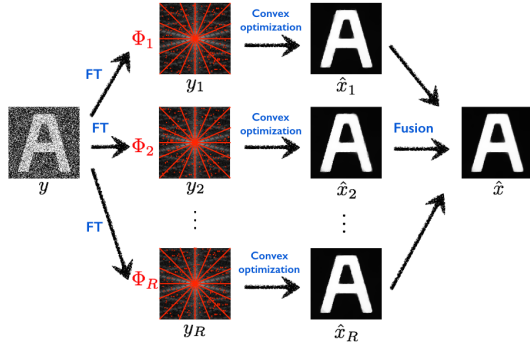


Fig. 1. Image simplification workflow. From a noisy image y , a given number of low-sampled measurement vectors y_k are generated, by taking the Fourier transform of y and selecting a subset of the Fourier coefficients (Φ_k). Then, each y_k is used to produce an estimator \hat{x}_k of the original signal through a convex optimization reconstruction scheme. Finally, all the \hat{x}_k are combined into an estimator \hat{x} .

2.1. Implementation

The proposed simplification method can be decomposed into four steps: (See Fig.1)

- *Generation of random subsets of measurement vectors y_k in the Fourier domain:* The OCT images that we want to simplify are known to have highly reflective interfaces between different layers of tissue. The layers are horizontal and somewhat parallel. We exploit this *a priori* information by using a star pattern to define the sampling operator Φ in the Fourier domain, as in [12]. To make sure that the principal direction of the layers is recovered, we run a first set of reconstructions using a uniform random sampling, and we use a Hough transform [13] on the resulting variance map (See eq.(3)). From the Hough accumulator we select the most probable line direction, independently of its position. This direction corresponds to a line of the star pattern. Other branches of that star pattern are positioned at regular angular intervals for a total of N_b branches. In practice, the principal direction of the layers in the Fourier domain is well recovered by an area slightly thicker than a line. Hence, if we denote by θ the angle of the principal line direction obtained with the Hough transform, the final star-shaped sampling pattern consists in the N_b regular branches, plus the cone of angles $\theta \pm \theta_\epsilon$, with $\theta_\epsilon = \frac{2\pi}{360}$. Finally, since we want the sample vectors y_k to be random, we add a set of random sampling positions uniformly distributed in the Fourier domain. (See Φ_k in Fig. 1)

The number of star branches and random samples in the operator Φ_k is controlled by the target sampling rate τ , so that if the image y is of size M , the measurement vectors y_k is of size τM . In this work we set $N_b = 16$ and $\tau = 0.05$ for drastic image simplification. An original component of our approach is to generate series of estimators \hat{x}_k from series of random samples y_k , ($k = 1, \dots, R$). We set here $R = 3$ and overall, the multiple samplings only use 8.7% of the Fourier domain.

- *Reconstruction of partial estimators \hat{x}_k through convex optimization:* We solve the classic convex optimization prob-

lem based on TV minimization, as proposed in [5]:

$$\hat{x}_k = \arg \min_x \|x\|_{TV} \quad \text{s.t.} \quad \|\Phi_k x - y_k\|_2 \leq \epsilon \quad (1)$$

using the NESTA algorithm [14]. The parameter ϵ is estimated using [14] and therefore depends on the noise variance and the sampling rate. Convergence of the algorithm is ensured since the operator Φ_k is such that $(\Phi_k^* \Phi_k)^2 = \Phi_k^* \Phi_k$.

- *Fusion of the \hat{x}_k to produce the mean image \hat{x}_{mean} and the variance map σ_x :* We aggregate the partial estimators via computation of their mean:

$$\hat{x}_{mean} = \frac{1}{R} \sum_{k=1}^R \hat{x}_k \quad (2)$$

The fused estimator \hat{x}_{mean} preserves the contrast of each reconstruction, and assigns them the same weight. We also define the variance map of the reconstructions as follows:

$$\sigma_x = \sqrt{\frac{1}{R-1} \sum_{k=1}^R (\hat{x}_k - \hat{x}_{mean})^2} \quad (3)$$

The map σ_x (illustrated in Fig. 4) reveals edge structures corresponding to the dissimilarities between the different partial estimators \hat{x}_k .

- *Adaptive reconstruction using both fusions and a local filter \mathcal{H} :* We finally define the simplified image \hat{x} as follows:

$$\hat{x} = (1 - \sigma_x) \circ \hat{x}_{mean} + \sigma_x \circ \mathcal{H}(y) \quad (4)$$

where \mathcal{H} represents a local smoothing filter applied on the original image y , and \circ is the entrywise product between two matrices. Here we used a simple 3×3 Gaussian filter.

3. EXPERIMENTAL RESULTS

3.1. OCT acquisition protocol and histological evaluation

We acquired the OCT images using a Telesto (Thorlabs, GmbH, Germany) commercial OCT system. Briefly, the system uses a 1325 nm center wavelength, a 150 nm bandwidth, a lateral resolution of $15 \mu m$ (in air), and an axial resolution of $6.5 \mu m$ (in air). Human hearts ($n = 4$) were obtained under the protocol from the National Disease Research Interchange (NDRI) [15]. In our experiment, we acquired B-scan images with of size 800×512 pixels, corresponding to $4mm \times 2.51mm$. Fresh samples were stored in phosphate buffered saline (PBS) and imaged within 48 hours of the donor's death. Upon OCT imaging, sections of samples were processed for histology. Sample pieces were cut parallel to the directions of the B-scans. After a fixation process in formalin and ethanol solution, the sample sections were stained with Masson Trichrome.

3.2. Image simplification of OCT images

We evaluated our algorithm on the dataset of 4 human hearts (See Fig.2) with the following characteristics:

- *Heart 1: One layer of constant thickness.* Such configuration is typical for human atrium tissue, where the regular layer corresponds to dense collagen.

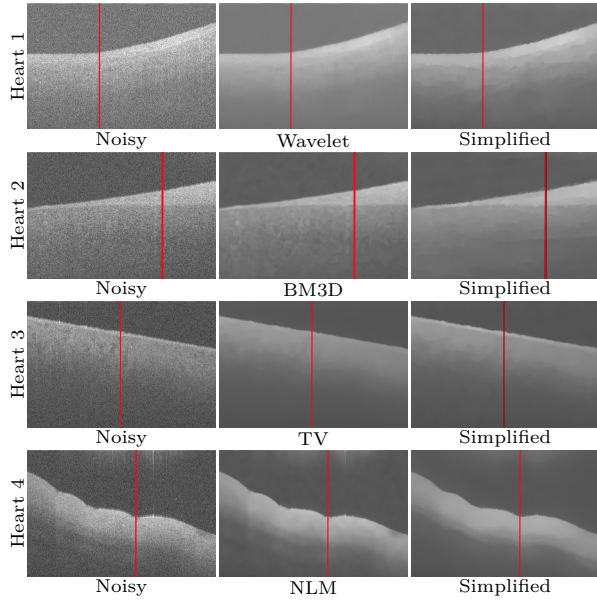


Fig. 2. Simplification of the heart images. For each noisy data, we present the result of our simplification algorithm, along with one of the 4 tested denoising methods: BM3D, Wavelet soft-thresholding, TV and NLM. See 3.3 for a detailed comparison of the results.

- *Heart 2: One layer of non-constant thickness.* Such configuration is typical of a diseased human ventricle tissue. The enlarged dense collagen layer is caused by myocardial scar.
- *Heart 3: One thin layer.* Such configuration is typical for healthy ventricular septum. The thin layer is the endothelium, and there is no dense collagen layer.
- *Heart 4: Two layers.* On some human atrium tissue, we can distinguish deeper layers, beyond the dense collagen in the first layer. They correspond to loose collagen, smooth muscle, or elastic tissues.

Each case is illustrated in Fig.2, where we show original OCT images and the simplified images.

3.3. Comparison to state of the art denoising

We show in Fig.2 outcomes of denoising using TV-filtering [10], Non-Local Means [16], Wavelet soft-thresholding [17] (which is one of the most common method used in OCT-image denoising [9]), and BM3D [18] (which is the reference for most denoising algorithms).

All four denoising methods performed badly for at least one of the cases, over-smoothing one layer (Heart 1, wavelet soft-thresholding; Heart 3, TV filtering), introducing strong visual artifacts such as oscillations (Heart 2 with BM3D; Heart 4 with NLM), patches (NLM) and staircasing (TV). On the other hand, our simplification method generated no artifacts and systematically preserved all visible layers.

Along with the simplified images, we compare vertical profiles from the different methods in Fig.3. We can see that some methods do not preserve the mean intensity inside each layer (e.g. TV) and that our proposed simplification returns

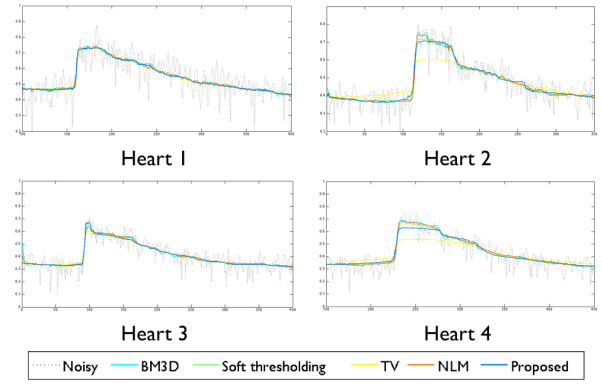


Fig. 3. Profiles of the Heart images. For each image, we represent the intensity along an axial line, for different reconstruction methods. We compare our method with 4 state-of-the-art denoising techniques.

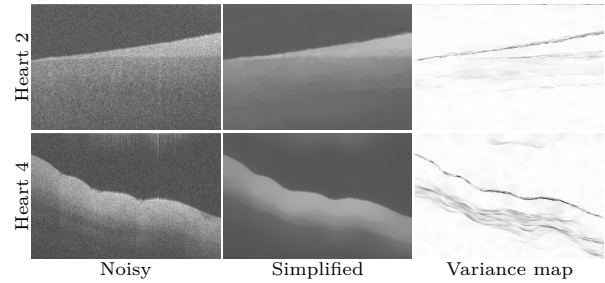


Fig. 4. Variance map of the Heart 2 and Heart 4 images, as defined in eq. (3). White areas correspond to $\sigma_x = 0$, and darker areas correspond to higher values of σ_x .

the profiles with the least oscillations. In every case, our method allows the determination of the number of layers as well as their thickness along a given profile, and preserves the mean intensity in each layer.

3.4. Application for layer segmentation

The proposed simplification method generates two outputs: the simplified image with layers preserved (in terms of positions and average intensity), and the variance map, with precise delineation of layer interfaces, corresponding to local disagreements between the reconstructions. Segmentation of layers can be performed on either one and we show in Fig. 5 some results exploiting local peak detection on vertical profiles of the variance map.

For each OCT image, we compared our segmentation results with the manual segmentation from an expert (See Tab.1). Histology images were also available and segmented manually, but the match between histology images and OCT cannot be assessed at the pixel level due to deformation (curving and shrinking) of tissue after chemical staining during histology.

In order to quantitatively evaluate our segmentation method, we computed the Root Mean Square (RMS) error between the manual and automated estimates of the average

Table 1. Average thickness (Th.) of the layers. Comparison between our method (Auto.), the manual segmentation of noisy OCT images (Manual) and the histology-based segmentation (Histo.). The 3 first columns represent the yellow layer from Hearts (H) 1 to 3, and the last two columns represent respectively the yellow (-1) and the green (-2) layer in Heart 4.

Th.(mm)	H1	H2	H3	H4 - 1	H4 - 2
Manual	0.152	0.174	0.044	0.273	0.170
Auto.	0.147	0.167	0.050	0.262	0.155
Histo.	0.059	0.195	0.025	0.323	0.153

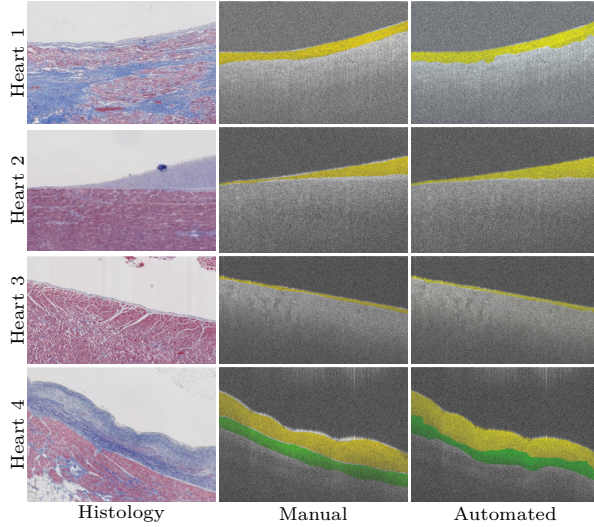


Fig. 5. Segmentation of the heart images. Histological images from each heart samples are displayed, along with Manual and Automated segmentation results overlaid on the raw SD-OCT images.

thickness of each layer appearing in the images. The RMS equals to $21 \mu\text{m}$, for a pixel size of $4.9 \mu\text{m}$. This very satisfying result confirms the efficiency of the variance map to precisely detect layers. In addition, the correlation between the thickness values from manual segmentation of SD-OCT and histology segmentation ($\rho_1 = 0.921$) is very close from the correlation between automated measures on the variance maps and the histology-based segmentation ($\rho_2 = 0.924$). This confirms that our results are consistent with those obtained through histopathological observations.

4. CONCLUSION

We have presented a sparsity-based image simplification method well suited for the study of myocardial tissue layers in OCT images. The proposed method was able to remove noise, preserve tissue layers intensities and positions, and generates a variance map which is directly exploitable for segmentation. The next step will focus on implementing such image simplification directly at the sensing stage, using multiple CS acquisitions. Such implementation is still not trivial, requiring open OCT systems to modify the sampling

scheme and hardware implementation of pseudo-random sampling patterns. Specifically, it is expected that the simplification scheme can be implemented in our customized OCT system [19]. In addition *a priori* information such as layer orientations and noise level will need to be inferred prior to acquisition.

5. REFERENCES

- [1] J.M. Schmitt, S.H. Xiang, and K.M. Yung, "Speckle in optical coherence tomography," *Journal of Biomedical Optics*, vol. 4, no. 1, pp. 95–105, 1999.
- [2] M. K. Garvin, M.D. Abramoff, Xiaodong Wu, S.R. Russell, T.L. Burns, and M. Sonka, "Automated 3-D intraretinal layer segmentation of macular spectral-domain optical coherence tomography images," *IEEE Transactions on Medical Imaging*, vol. 28, pp. 1436–1447, 2009.
- [3] Q. Yang, C.A. Reisman, Z. Wang, Y. Fukuma, M. Hangai, N. Yoshimura, A. Tomidokoro, M. Araie, A.S. Raza, D.C. Hood, and Chan K., "Automated layer segmentation of macular OCT images using dual-scale gradient information," *Opt. Express*, vol. 20, no. 18, pp. 21293–21307, 2010.
- [4] A. Mishra, A. Wong, K. Bizheva, and D.A. Clausi, "Intra-retinal layer segmentation in optical coherence tomography images," *Opt. Express*, vol. 26, no. 17, pp. 23719–23728, 2009.
- [5] E.J. Candès, J. Romberg, and T. Tao, "Robust uncertainty principles: Exact signal reconstruction from highly incomplete frequency information," *IEEE Transactions on Information Theory*, vol. 52, no. 2, pp. 489–509, 2006.
- [6] L. Fang, S. Li, Q. Nie, J.A. Izatt, C.A. Toth, and S. Farsiu, "Sparsity based denoising of spectral domain optical coherence tomography images," *Biomed. Opt. Express*, vol. 3, no. 5, pp. 927–942, 2012.
- [7] X. Liu and J. U. Kang, "Compressive SD-OCT: the application of compressed sensing in spectral domain optical coherence tomography," *Optics Express*, vol. 18, no. 21, pp. 22010–22019, 2010.
- [8] M. Gargesha, M. W. Jenkins, A. M. Rollins, and D. L. Wilson, "Denoising and 4D visualization of OCT images," *Opt. Express*, vol. 16, no. 16, pp. 12313–12333, 2008.
- [9] M.A. Mayer, A. Borsdorf, M. Wagner, J. Hornegger, C.Y. Mardin, and R.P. Tornow, "Wavelet denoising of multiframe optical coherence tomography data," *Optics Express*, vol. 3, no. 3, pp. 572–589, 2012.
- [10] L. I. Rudin, S. Osher, and E. Fatemi, "Nonlinear total variation based noise removal algorithms," *Phys. D*, vol. 60, no. 1-4, pp. 259–268, 1992.
- [11] W. Meinel, E. Angelini, and J.-C. Olivo-Marin, "Image denoising by adaptive compressed sensing reconstructions and fusions," in *Proc. SPIE*, August 2015.
- [12] Z. Wang and G.R. Arce, "Variable density compressed image sampling," *IEEE Transactions on Image Processing*, vol. 19, no. 1, pp. 264–270, 2010.
- [13] R.O. Duda and P.E. Hart, "Use of the Hough transformation to detect lines and curves in pictures," *Commun. ACM*, vol. 15, no. 1, pp. 11–15, 1972.
- [14] S. Becker, J. Bobin, and E. Candès, "Nesta: A fast and accurate first-order method for sparse recovery," *SIAM Journal on Imaging Sciences*, vol. 4, no. 1, pp. 1–39, 2011.
- [15] Y. Gan, D. Tsay, S.B. Amir, C.C. Marboe, and C.P. Hendon, "Automated classification of optical coherence tomography images of human atrial tissue," *Submitted to Journal of Biomedical Optics*, 2015.
- [16] A. Buades, B. Coll, and J.-M. Morel, "A review of image denoising algorithms, with a new one," *Multiscale Modeling & Simulation*, vol. 4, no. 2, pp. 490–530, 2005.
- [17] D. L. Donoho, "De-noising by soft-thresholding," *IEEE Transactions on Information Theory*, vol. 41, no. 3, pp. 613–627, 1995.
- [18] K. Dabov, A. Foi, V. Katkovnik, and K. Egiazarian, "Image denoising by sparse 3D transform-domain collaborative filtering," *IEEE Transactions on Image Processing*, vol. 16, no. 8, pp. 2080–2095, 2007.
- [19] X. Yao, Y. Gan, C.C. Marboe, and C.P. Hendon, "Myocardial imaging using ultrahigh resolution spectral domain optical coherence tomography," *Submitted to Journal of Biomedical Optics*, 2015.